Liquid ropes: a geometrical model for thin viscous jet instabilities

P.-T. Brun,[1,2,3,4] Basile Audoly,[1] Neil M. Ribe,[2] T. S. Eaves,[5] and John R. Lister[5]

[1] *CNRS and UPMC Univ. Paris 06, UMR 7190, Institut Jean le Rond d'Alembert, Paris, France*
[2] *Laboratoire FAST, Université Paris-Sud, CNRS, Bâtiment 502, Campus Universitaire, Orsay 91405, France*
[3] *Laboratory of Fluid Mechanics and Instabilities, EPFL, CH1015 Lausanne, Switzerland*
[4] *Department of Mathematics, Massachusetts Institute of Technology, Cambridge, Massachusetts 02139, USA*
[5] *Institute of Theoretical Geophysics, Department of Applied Mathematics and Theoretical Physics, University of Cambridge, Wilberforce Road, Cambridge CB3 0WA, UK*

(Dated: March 16, 2015)

Thin viscous fluid threads falling onto a moving belt behave in a way reminiscent of a sewing machine, generating a rich variety of periodic stitch-like patterns including meanders, W-patterns, alternating loops, and translated coiling. These patterns form to accommodate the difference between the belt speed and the terminal velocity at which the falling thread strikes the belt. Using direct numerical simulations, we show that inertia is not required to produce the aforementioned patterns. We introduce a quasi-static geometrical model which captures the patterns, consisting of three coupled ODEs for the radial deflection, the orientation and the curvature of the path of the thread's contact point with the belt. The geometrical model reproduces well the observed patterns and the order in which they appear as a function of the belt speed.

PACS numbers: 47.54.-r, 47.20.-k, 47.85.Dh, 46.32.+x

No-one who has played with pouring honey from a spoon onto toast can fail to have been fascinated by the peculiar dynamics of coiling and folding of the viscous stream on impact. This surprisingly complex behavior can be reproduced in a simple yet well-controlled experiment, where a viscous thread falls onto a moving belt: the patterns laid down by the thread are diverse, and include meanders, alternating loops, W-pattern, coiling (Fig. 1), as well as various resonant patterns such as double coils and double meanders [1–3]. This system has been thoroughly studied [1–5] but lacks a simple explanation until now. The resemblance of these patterns to the stitch patterns of a sewing machine led [1] to call the system the "fluid mechanical sewing machine" (FMSM). Some patterns (see Fig. 1a) produce evenly spaced self-intersections which can serve as sacrificial bonds [6]: solidified fibers containing such a micro-structure display a combination of high toughness and stretchability, revealed by mechanical tests [7], as they effectively reproduce nature's design for spider silk [8]. Similar coiling patterns can be found in a number of industrial or everyday situations, such as the production of non-woven textiles [9], the laying down of "squiggles" of icing on cakes, Jackson Pollock's action painting, in which paint from a moving brush dribbles onto a stationary horizontal canvas [10], or when transoceanic fiber-optic cables are deposited from a vessel onto the ocean bed [11]. The latter are elastic rather than viscous [12–14], showing that the patterns are robust with respect to a change in the thread rheology.

In this Letter, we show that the patterns can be described quantitatively by a non-linear ordinary differential equation which depends on three state variables only, and is geometric in essence. This model builds upon previous work which revealed a connection between

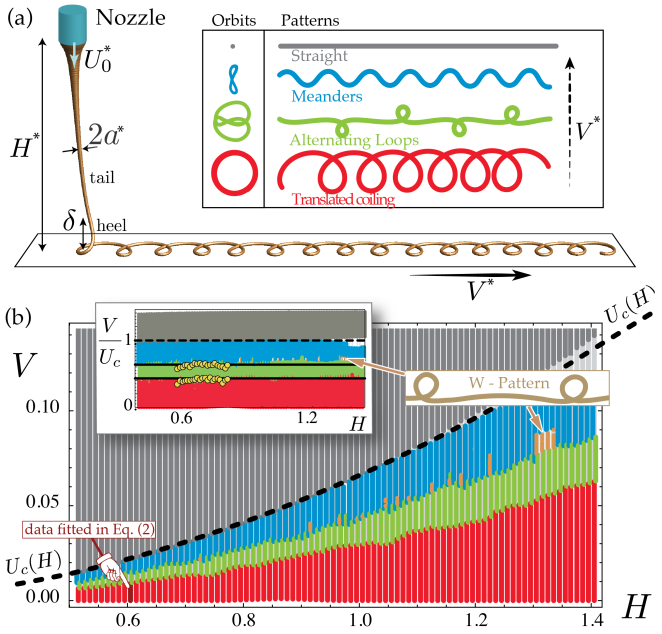

FIG. 1. (a) Direct numerical simulation, with no inertia, of a thin thread of viscous fluid falling from a height H^* onto a belt of velocity V^*. Shown are four periodic orbits of the contact point of the thread on the belt, and the corresponding spatial patterns. (b) Phase diagram showing the distribution of patterns in the *dimensionless* parameter plane (H, V). The speed $U_c(H)$ at which the fluid coils in the absence of advection $(V = 0)$ is shown by the dashed line. Inset: same diagram, with belt velocity rescaled by coiling velocity $U_c(H)$. The yellow dots correspond to experimentally measured thresholds [3].

the FMSM patterns and the well-studied case of steady-coiling: in the laboratory frame, the motion of the point where the thread makes contact with the belt involves multiples or simple ratios of the steady-coiling frequency Ω_c [5]. Accordingly, our geometric model uses the position of this point as a state variable, as well as the direction of the tangent to the thread. Before deriving the model we perform direct simulations of the FMSM with the Discrete Viscous Rods algorithm (DVR) [4, 5] to propose a rationalization of the FMSM phase diagram when inertia is negligible, *i.e.* for moderate fall heights. Since this DVR algorithm is known to accurately predict the experimental FMSM patterns [4, 5], we will not repeat a detailed comparison with experiments here.

Consider a thread with kinematic viscosity ν falling at a volumetric rate Q^* from a nozzle of dimensional height H^* onto a conveyor belt moving horizontally at speed V^*. The thread is stretched by gravity (denoted g) during its fall so that the speed of the fluid increases with distance from the nozzle. Balancing the gravitational stretching with the viscous dissipation yields a typical length scale $(\nu^2/g)^{1/3}$ and time scale $(\nu/g^2)^{1/3}$ that we use to nondimensionalize our equations. In particular, $H = H^*(g/\nu^2)^{1/3}$ and $V = V^*/(\nu g)^{1/3}$ are the dimensionless height of fall and belt velocity, respectively. By varying these two parameters, one generates a phase diagram for the FMSM [5]. Herein, we work with the typical parameter values used in the literature [2, 3] such that $0.5 \leqslant H \leqslant 1.4$. We artificially omit inertia in our simulations, an assumption which is valid in almost this entire range (specifically, for $H \leqslant 1.2$, see §1 in S.I.) By doing so, we find that all the simple patterns survive in this quasi-static limit, see Fig. 1, thereby confirming that inertia is irrelevant for moderate fall heights.

When the belt has velocity $V = 0$ the thread coils steadily with a radius R_c, frequency Ω_c and speed $U_c = R_c\Omega_c$ (steady coiling) [15]. When gradually increasing the belt velocity while keeping other parameters constant, the coiling pattern is first simply translated on the belt (translated coiling) up to a certain critical value of V where loops form alternatively on one side of the belt and then the other (alternating loops). For higher belt speeds the thread exhibits some meanders [16, 17] which collapse to a straight line for a critical value of the belt velocity V_c. For velocities higher than V_c the thread has a catenary shape and its contact point with the belt is stationary in the laboratory frame. In the rest of the Letter we concentrate on belt speeds in the range $0 \leqslant V \leqslant V_c$. Three points are of particular interest. First, no double patterns [5] such as the double coiling or double meanders were found in these quasi-static conditions. This was anticipated since such resonant patterns are typically observed for large values of H where inertia is dominant in normal conditions [5]. Second, we found hysteresis in the critical belt velocity values corresponding to the transition between patterns. The data shown in Fig. 1b are for a slowly accelerating belt. The case of a decelerating belt is discussed at the end of the Letter. Third, we report the presence of another pattern, the W-pattern, which we found in limited portions of the diagram (see overlay in Fig. 1b). It appears in competition with the meanders after the alternating loops become unstable when the belt speed is increased, and only then.

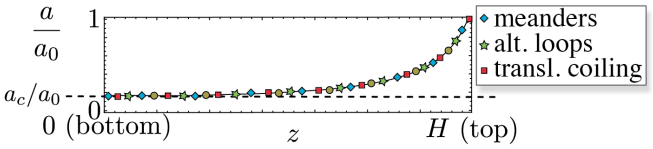

FIG. 2. The thread's radius distribution $a(z)$ normalized by the nozzle's radius a_0 is identical for any pattern in the range $V < V_c$. Stretching is limited to the upper part of the thread, and the radius is constant near the belt.

For any height H, we can compute the steady coiling velocity $U_c \equiv R_c\Omega_c$ using the method of [18]. This yields the dashed curve in Fig. 1b. The curve matches the lower boundary of the grey region (straight pattern), which reveals that the onset of steady coiling matches accurately the critical velocity $V_c = U_c$. The central role played by the reduced velocity V/U_c in the formation of the patterns becomes even more evident when one plots the phase diagram in terms of V/U_c, see inset in Fig 1b: then, all boundaries between patterns become horizontal straight lines. This important finding shows that the only influence of the height of fall on the patterns is to set the value of the reduced velocity $V/U_c(H)$: the patterns can be rationalized strictly in terms of the parameter $V/U_c(H)$. This is confirmed by the collapse of the experimental measurements from Ref. [3] (for low fall heights hence negligible inertia) onto horizontal bands in Fig 1b.

The reason why V/U_c is the only relevant parameter may be understood by analyzing the thread's radius profile $a(z)$ for different V while keeping H constant, *i.e.* moving vertically in the phase diagram and browsing through the different patterns. We do so in Fig 2 and find that all the curves $a(z)$ collapse onto a single master curve. In the upper part of the master curve, called the tail, the thread is accelerated and stretched by gravity until it reaches a terminal radius a_c. Both this radius and the speed $Q/(\pi a_c^2)$ at which the thread arrives on the belt are found to be approximately independent of V in the range $0 \leqslant V \leqslant V_c$. As a consequence the thread speed may be called the free-fall speed [1] and is equal to the coiling speed U_c (observed when $V = 0$) which solely depends on H. In general U_c and V do not match and there is a small region near the lower end of the thread, called the heel in Fig.1, where the thread bends and twists while keeping a constant radius. The patterns are produced as the heel is set in motion to satisfy the no-slip boundary condition at the contact point between thread and belt:

$$U_c\,\mathbf{t} + V\,\mathbf{e}_x = \dot{\mathbf{r}} \tag{1}$$

Here we use the notation introduced in Fig. 3: $\mathbf{t}$ is the

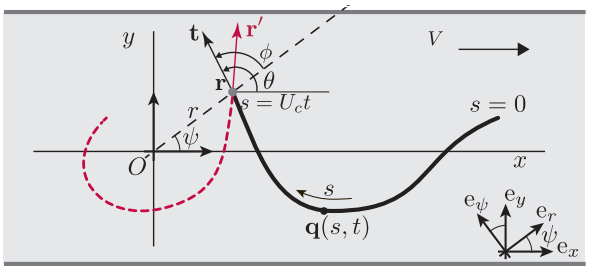

FIG. 3. Geometrical model, in the plane of the belt: trace $\mathbf{q}$ (thick black curve) with arc-length s, orbit of the contact point (dashed red curve), and projection O of the nozzle onto the belt's plane. The curvature of the thread is assumed to be a function of the polar coordinates (r, ϕ) of the point of contact $\mathbf{r}$.

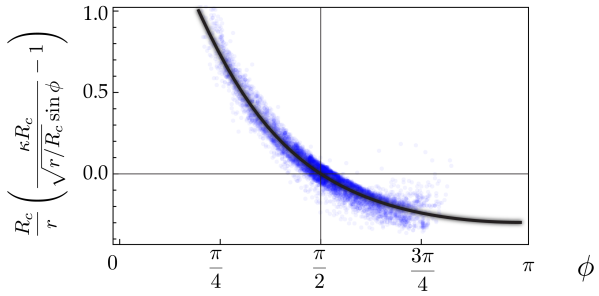

FIG. 4. Collapse of the DVR simulation data for the rescaled curvature as a function of ϕ, for the translated coiling pattern ($H = 0.6$ and $0 < V/U_c < 0.4$, see darker red bar in the lower left corner of Fig. 1b). See Supplementary Information for details.

unit tangent to the thread at the point of contact $\mathbf{r}$ with the belt, $\dot{\mathbf{r}}$ is the velocity in the laboratory frame of this non-material point, and $\mathbf{e}_x$ is a unit vector in the direction of belt motion. The limiting case of steady coiling corresponds to $V = 0$ and $\dot{\mathbf{r}} = U_c\,\mathbf{t}$, and the case of a straight (catenary) pattern corresponds to $\dot{\mathbf{r}} = \mathbf{0}$, $\mathbf{t} = -\mathbf{e}_x$ and $V = U_c$. In the general case $V/U_c < 1$, the speed at which the thread arrives at the belt exceeds the belt's ability to carry it away in a straight line ($\dot{\mathbf{r}} \neq \mathbf{0}$ in equation above). This excess length of thread is accumulated on the belt in the form of patterns produced as the heel lays down on the belt. This agrees with our initial observation that the critical velocity at which the straight pattern appears is $V_c = U_c$, see Fig 1b.

We now turn to the task of characterizing and modeling the heel boundary layer where the deposition takes place. Since bending stresses are dominant in the heel, we anticipate that the curvature κ of the thread at the point of contact plays a key role in the pattern formation. Working in the quasi-static (inertialess) limit, we assume that the shape of the hanging thread (and in particular its curvature near the point of contact) is only a function of the current boundary conditions applied to the thread. The boundary conditions at the nozzle are time-invariant as the fall height and flow rates are fixed. Therefore, we view the curvature κ at the bottom of the hanging thread as a function of the position $\mathbf{r}$ of the point of contact and the orientation of the tangent $\mathbf{t}$. The equations for the hanging thread are cylindrically invariant, and therefore we have $\kappa = \kappa(r, \phi)$, where ϕ is the direction of the tangent relative to the line joining the projection of the nozzle O to the point of contact $\mathbf{r}$ (Fig. 3). The function $\kappa(r, \phi)$ is found by fitting DVR simulations of translated coiling for the case $H = 0.6$ and $0 < V/U_c < 0.4$ (darker red bar in the lower left corner of Fig. 1b). As explained in the S.I., §2.1, time series of (r, ϕ, κ) for the translated coiling pattern are well approximated by the heuristic fit

$$\kappa(r, \phi) = \frac{1}{R_c}\sqrt{\frac{r}{R_c}}\left(1 + A(\phi)\,\frac{r}{R_c}\right)\sin\,\phi \qquad (2)$$

where $A(\phi) = b^2\cos\phi/(1 - b\cos\phi)$ and $b = 0.715$ and R_c is the radius of steady coiling [15]. Fig 4 shows the collapse of the numerical data obtained from Eq. (2). The result of this fitting procedure is robust with respect to the particular value of H chosen (see §2.2 in the S.I.)

Building on our previous observations, we now derive a quasi-static geometric model for the formation of the trace. The heel is modeled as a filament of uniform radius falling towards the belt at a velocity U_c, which is bent and laid down quasi-statically onto the belt. Let s be the arc-length along the trace, with $s = 0$ corresponding to the point which contacted the moving belt at time $t = 0$ and $s = U_c t$ corresponding to the current point of contact $\mathbf{r}$. We label material points in the trace by their (Lagrangian) coordinate s. We also use s as a time-like variable and write $\mathbf{r}(s)$ for the contact position at time $t = s/U_c$. Let $\mathbf{q}(s, t)$ be the position on the belt of the point s at time t, with $0 \le s \le U_c t$. This point was deposited at time s/U_c at position $\mathbf{r}(s)$, and has subsequently been advected at velocity $V\mathbf{e}_x$ by the belt. Thus

$$\mathbf{q}(s, t) = \mathbf{r}(s) + V\,(t - s/U_c)\,\mathbf{e}_x. \qquad (3)$$

In our model of the thread, the dynamical quantities of interest are the contact position $\mathbf{r}$, and the tangent vector $\mathbf{t}$ and curvature κ at the point of contact. At any point s, the tangent to the trace is $\partial\mathbf{q}/\partial s$. In particular, at the point of contact $\mathbf{t}(s) = \partial\mathbf{q}/\partial s|_{s=U_c\,t} = \mathbf{r}'(s) - V/U_c\,\mathbf{e}_x$, and we recover Eq. (1) with $\mathbf{r}' = \dot{\mathbf{r}}/U_c$. Now let $(r(s), \psi(s))$ denote the polar coordinates of the contact point $\mathbf{r}(s)$ as shown in Fig. 3, and let $\theta(s)$ denote the angle from the x-axis to $\mathbf{t}(s)$. We resolve $\mathbf{r}'$, $\mathbf{t}$ and $\mathbf{e}_x$ into the polar basis $(\mathbf{e}_r, \mathbf{e}_\psi)$, and use $\phi = \theta - \psi$ to eliminate the dependence on ϕ:

$$r' = \cos(\theta - \psi) + \frac{V}{U_c}\,\cos\psi \qquad (4a)$$

$$r\,\psi' = \sin(\theta - \psi) - \frac{V}{U_c}\,\sin\psi. \qquad (4b)$$

Finally, θ' is the curvature of the trace at the contact point, which has been found in Eq. (2) in terms of a

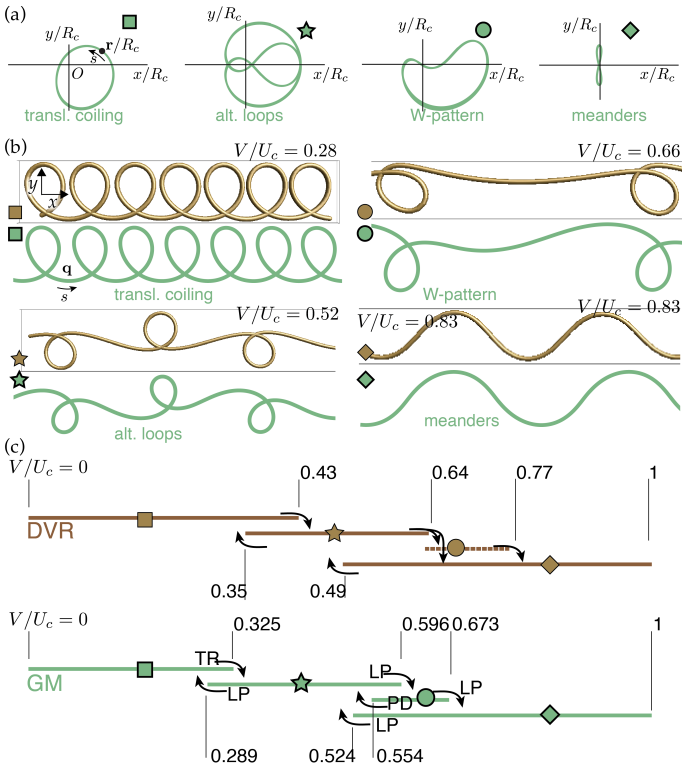

FIG. 5. (a) The four periodic orbits $\mathbf{r}(s)$ obtained with the GM and (b) the corresponding patterns $\mathbf{q}(s,t)$ (green), compared to the pattern obtained with DVR simulations (brown) for identical ratios V/U_c. (c) Patterns encountered with DVR while quasi-statically increasing the ratio V/U_c (resp. decreasing, as indicated by the arrows) along with the stability domains and bifurcation analysis computed with the GM (green): period doubling (PD), fold point (LP), torus bifurcation (TR).

fitting function κ:

$$\theta' = \kappa(r, \theta - \psi). \tag{4c}$$

Equations (4a–4c) are a set of coupled ordinary nonlinear differential equations for the functions $r = r(s)$, $\psi = \psi(s)$ and $\theta = \theta(s)$, depending on a *single* dimensionless parameter V/U_c — the parameter R_c in equation (2) sets a lengthscale for r and s, and can be removed by rescaling. We refer to this system of differential equations as the *geometrical model* (GM). The kinematic equations (4a–4b) capture the coupling with the moving belt, while equation (4c) captures the shape of the hanging thread as set by the balance of viscous forces and gravity. We integrated the GM numerically, varying the velocity parameter in the range $0 \leqslant V/U_c \leqslant 1$ (Fig 5). The solutions $\mathbf{r}(s)$ were found to settle into periodic orbits, see Fig. 5a. The patterns corresponding to the different orbits can be identified by reconstructing the complete trace $\mathbf{q}$ from Eq. (3), and then compared to those obtained by DVR simulations, see Fig. 5b. With the aim to calculate the bifurcation thresholds accurately and to identify the nature of the bifurcations, we also investigated the stability domains of the periodic solutions of the GM using the continuation software AUTO 07p [19], see Fig. 5c.

All the patterns originally observed with DVR in the quasi-static (non-inertial) limit are captured by the GM. They appear in the correct order when V/U_c is varied, and there is a good agreement on the values of the pattern boundaries, see Fig. 5c. Their shapes are accurately captured as well, see Fig. 5b. Alternating loops and meanders are symmetric about $y = 0$ in their full domain of existence, both in DVR simulations and in the GM. The alternating loops, and the amplitude of meanders both decrease as the belt velocity increases and the latter tends to zero when $V = U_c$, as expected. Coils are symmetric at zero belt velocity, but then turn asymmetric at larger velocities. W-patterns are, on the other hand, always asymmetric.

Interestingly, the GM sheds light on two subtle features of the FMSM. First, it accounts for the hysteresis observed in DVR when transitions between patterns occur at different values depending on whether the belt velocity is increasing or decreasing: the domains of stability of the various patterns predicted by the GM do indeed overlap, see Fig. 5c. Second, it explains why the W-pattern can be observed in DVR with an increasing belt velocity, but not with a decreasing one. Indeed, the layout of the stability diagram of the GM in Fig. 5c predicts that meanders will destabilize directly into alternated loops for a decreasing belt velocity, skipping the W-pattern.

The geometrical model is formulated as an evolution problem for the position of the contact point, with an additional dependence on the tangent orientation. This dependence induces a memory effect which explains the complexity of the patterns, even in the absence of inertia. The central role of geometry explains the robustness of the patterns with respect to the rheology of the thread. By condensing the dynamics of the spatially extended thread to that of a single point, we could interpret the patterns using methods from the field of dynamical systems, rather than pattern formation [20]. From the point of view of applications, the FMSM suits the inertialess environment associated with fabrication at the micro-scale [21]. Modulating the orientation and lateral position of the belt or nozzle offers an interesting avenue to extend the library of patterns, thereby offering a possible alternative to 3D printing [22] and electrospinning [23]: our GM allows these modulations to be designed in a rational way.

[1] S Chiu-Webster and J R Lister. *J. Fluid Mech.*, 569, 2006.

[2] S. W. Morris, J. H. P. Dawes, N. M. Ribe, and J. R.

Lister. *Phys. Rev. E*, 77(6), 2008.
[3] R. Welch, B. Szeto, and S. Morris. *Phys. Rev. E*, 85(6):066209, 2012.
[4] B. Audoly, N. Clauvelin, P.-T. Brun, M. Bergou, E. Grinspun, and M. Wardetzky. *J. Comp. Phys.*, 253:18–49, 2013.
[5] P.-T. Brun, N. M. Ribe, and B. Audoly. *Phys. Fluids*, 24(4):043102, 2012.
[6] F. P. Gosselin, D. Therriault, and M. Levesque. In *APS Meeting Abstracts*, volume 1, page 52009, 2012.
[7] R. Passieux, D. Therriault, and F. Gosselin. Creation of sacrificial bonds by viscous flow instability. *Proceedings of the IMECE2014, ASME*, 2014.
[8] N. Becker, D. Oroudjev, S. Mutz, J. P. Cleveland, P. K. Hansma, C. Y. Hayashi, D. E. Makarov, and H. G. Hansma. *Nature materials*, 2(4):278–283, 2003.
[9] N. Marheineke and R. Wegener. *J. Fluid Mech.*, 622, 2009.
[10] A. Herczyński, C. Cernuschi, and L. Mahadevan. *Phys. Today*, 64, 2011.
[11] L. Carter. *Submarine cables and the oceans: connecting the world*. Number 31. UNEP/Earthprint, 2009.
[12] M. Habibi, J. Najafi, and N. M. Ribe. *Phys. Rev. E*, 84(1), 2011.
[13] M. Bergou, M. Wardetzky, S. Robinson, B. Audoly, and E. Grinspun. *ACM Trans. Graphics*, 27(3):63:1–63:12, 2008.
[14] M. K. Jawed, F. Da, J. Joo, E. Grinspun, and P. M. Reis. Coiling of elastic rods on rigid substrates. *Proceedings of the National Academy of Sciences*, 111(41), 2014.
[15] N. M. Ribe, M. Habibi, and D. Bonn. Liquid rope coiling. *Annu. Rev. Fluid Mech.*, 44, 2012.
[16] N. M. Ribe, J. R. Lister, and S. Chiu-Webster. *Phys. Fluids*, 18(12), 2006.
[17] M. J. Blount and J. R. Lister. *J. Fluid Mech.*, 674:489–521, 2011.
[18] N. M. Ribe. *Philos. T. Roy. Soc. A*, 460(2051), 2004.
[19] E. Doedel, A. R. Champneys, T. F. Fairgrieve, Y. A. Kuznetsov, B. Sandstede, and X. J. Wang. Available at http://indy.cs.concordia.ca/auto/, 2002.
[20] M. C. Cross and P. C. Hohenberg. *Rev. Mod. Phys.*, 65:851–1112, 1993
[21] J. Pfahler, J. Harley, H. Bau, and J. Zemel. *Sensors and Actuators A: Physical*, 22(1):431–434, 1989.
[22] D. Therriault, S. R. White, and J. A. Lewis. *Nature Materials*, 2(4):265–271, March 2003.
[23] A. L. Yarin, B. Pourdeyhimi, and S. Ramakrishna. *Fundamentals and Applications of Micro and Nanofibers* Cambridge University Press, 2014.

Supplemental material for 'Liquid ropes: a geometrical model for thin viscous jets instabilities'

P.-T. Brun, B. Audoly, N. M. Ribe, T. S. Eaves, J. R. Lister

March 13, 2015

1 Influence of inertia on the FMSM patterns

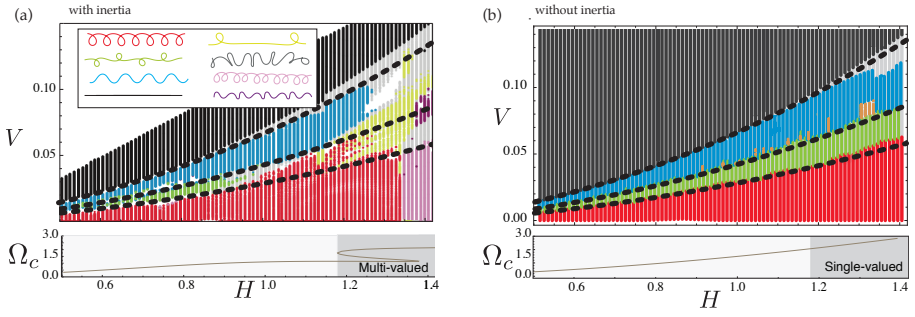

Figure 1: Phase diagrams obtained with the DVR numerical method using the same set of numerical parameters as in Ref. [13]: (a) with inertia and (b) without inertia. The set of dotted curves are identical across subfigures (a) and (b), and indicate the pattern boundaries in the absence of inertia: they closely match the boundaries with inertia, see (a), up to a dimensionless fall height $H \approx 1.2$. Below the phase diagrams, the steady coiling frequency Ω_c is plotted as a function of the fall height H: the region $H \geq 1.2$ where inertia has an influence on steady coiling is highlighted in dark grey.

With the aim to assess the influence of inertia on the FMSM patterns, we produced two phase diagrams using the DVR algorithm, see figure 1: one with inertia (as in Ref. [5] cited in main text, which was shown to give good agreement with experiments), and another without inertia (as in the main text of the present work). Up to a dimensionless fall height $H \approx 1.2$, the role of inertia appears to be negligible. Beyond $H \approx 1.2$, inertia leads to the formation of complex patterns by period doubling, and the phase diagrams differ.

The reason why inertia affects the patterns beyond the particular value $H \approx 1.2$ can be understood based on the plots for the steady coiling frequency, shown in the bottom of figure 1 (steady coiling corresponds to a belt at rest, $V = 0$). For low heights of fall, inertia plays no role as the coiling frequency is set by the balance of viscous and gravitational effects in both the coil and the upper part of the thread: Ω_c is then single valued (as shown in the bottom of figure 1a), and unaffected when we turn off inertia (compare with the bottom of figure 1b). For larger fall heights $H \gtrsim 1.2$, however, a multivalued regime is found, see shaded region in the bottom of figure 1a. This multivalued regime arises when the pendulum modes of the upper part of the thread enter in resonance with the excitation coming from the heel. The pendulum modes rely on inertia and are suppressed when inertia is omitted in the simulation: accordingly, the curve $\Omega_c(H)$ remains single-valued in the shaded region in the bottom of figure 1b. The complex patterns obtained by period doubling, shown in the phase diagram with inertia in part (a) of the figure, also result from an interaction of the motion of the heel with the pendulum modes, see Ref. [5] cited in main text. They appear beyond $H \approx 1.2$ in the presence of inertia, and are never found when inertia is turned off.

2 A formula fitting the curvature obtained in numerical simulations of translated coiling

2.1 Fitting procedure

We present a detailed derivation of the empirical fitting law that we introduced in Eq. (2) of the main text.

We first collected numerical data by running the Discrete Viscous Rod method (DVR) over a range of parameters where the translated coiling pattern is observed ($H = 0.6$ and $0 < V/U_c < 0.4$). This pattern was chosen as it sweeps a significant region in the parameter space (r,ϕ). The particular choice of the parameter value $H = 0.6$ has little influence on the final result, see §2.2 below.

We recorded a time series for the quantities (r, ϕ, κ) which are defined in figure 3 of the main text: r is the distance of the point of contact with the belt to the vertical projection O of the nozzle onto the belt, ϕ is the angle between radial direction (from O to the point of contact) and the tangent to the thread, and κ is the curvature of the projection of the thread's centerline onto the plane of the belt at the point of contact. We then used the value of the coiling radius R_c relevant to the height $H = 0.6$ to nondimensionalize r and κ. The rescaled radius and curvature are defined by

$$\overline{r} = \frac{r}{R_c} \quad \overline{\kappa} = \kappa\, R_c. \tag{1}$$

A fitting law $\overline{\kappa}(\overline{r}, \phi)$ for the numerical data $(\overline{r}, \phi, \overline{\kappa})$ was obtained as follows. We observed that the isolines of the quantity ϕ are very close to straight lines

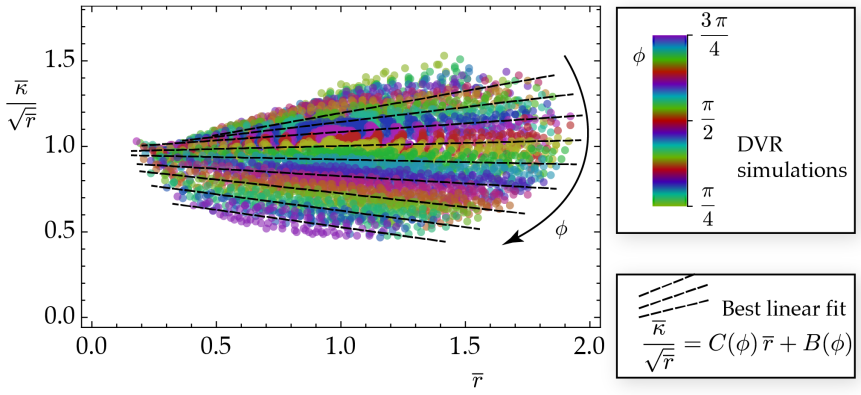

Figure 2: Simulation data for translated coiling from DVR, showing isolines for ϕ (coloring) in the $\left(\overline{r}, \frac{\overline{\kappa}}{\sqrt{\overline{r}}}\right)$ plane.

when plotted in the plane $\left(\overline{r}, \frac{\overline{\kappa}}{\sqrt{\overline{r}}}\right)$, see figure 2. For any target value of ϕ, we collected the numerical samples $(\overline{\kappa}, \overline{r})$ whose corresponding ϕ matches the target ϕ up to a small error $\epsilon \ll 1$, and made a linear fit for $\frac{\overline{\kappa}}{\sqrt{\overline{r}}}$ as a function of $\overline{r}$:

$$\frac{\overline{\kappa}}{\sqrt{\overline{r}}} \approx C(\phi)\,\overline{r} + B(\phi) \quad \text{(best linear fit for fixed } \phi\text{)}. \tag{2}$$

These linear fits correspond to the dashed lines shown in figure 2 (not all the fits are shown in the figure for the sake of legibility).

In figure 3, we show that the constant term in the fitting law in Eq. (2) is very well approximated by a sine function with no adjustable parameter,

$$B(\phi) \approx \sin\phi. \tag{3}$$

The choice of the sine function is compatible with the symmetries of the system. Indeed, in the absence of inertia the viscous hanging thread is invariant by a mirror symmetry with respect to the vertical plane (Orz) containing the nozzle and the point of contact. As a result, $\overline{\kappa}(\overline{r}, \theta)$ is an odd function of θ, and so are $B(\phi)$ and $C(\phi)$. Note that both the original data $(\phi, B(\phi))$ (red dots) and the *symmetrized* data $(-\phi, -B(\phi))$ (blue dots) are fitted in figure 3.

Combining the previous fits, we find

$$\overline{\kappa} \approx \sqrt{\overline{r}}\,\left(1 + A(\phi)\,\overline{r}\right)\,\sin\phi. \tag{4}$$

The fitting function $A(\phi) = \frac{C(\phi)}{B(\phi)}$ is found as follows. We plot the numerical data from DVR in the plane $\left(\phi, \frac{1}{\overline{r}}\left(\frac{\overline{\kappa}}{\sqrt{\overline{r}}\,\sin\phi} - 1\right)\right)$, as shown in figure 4. Note that $\frac{1}{\overline{r}}\left(\frac{\overline{\kappa}}{\sqrt{\overline{r}}\,\sin\phi} - 1\right)$ is the value of $A(\phi)$ predicted by equation (4). The collapse of

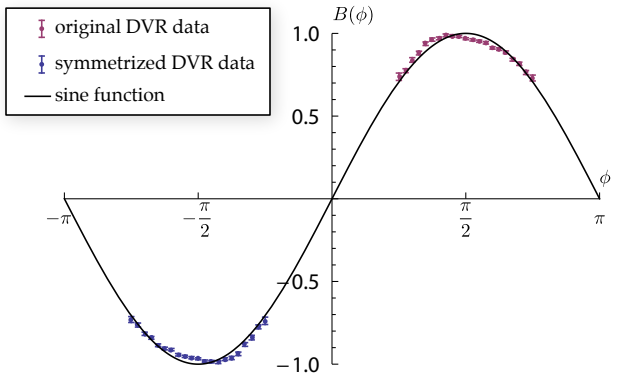

Figure 3: Fit of the constant coefficient $B(\phi)$ by a sine function.

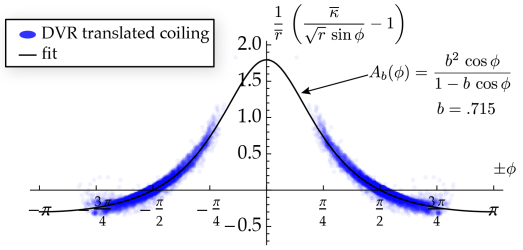

Figure 4: Fitting the quantity $A(\phi)$ in equation (4).

the simulation data onto a master curve confirms our previous fits. In view of the fact that $A(\phi)$ is an even function, we fit both the original cloud of points coming from the DVR simulation, and the set obtained by mirror symmetry with respect to the vertical axis ($\phi \to -\phi$ symmetry).

We used a fitting function having a single adjustable parameter b:

$$A_b(\phi) = \frac{b^2 \cos\phi}{1 - b\cos\phi}. \tag{5}$$

This choice is consistent with the fact that $A(\phi)$ is an even function.

It is also consistent with the existence of the steadily coiling solution, as we now show. In our units, the steadily coiling solution corresponds to $(\overline{r}, \phi, \overline{\kappa}) = (1, \pm\pi/2, 1)$: inserting this into equation (4) yields $A(\pm\pi/2) = 0$. In figure 4, the cloud of numerical data indeed passes through the points $(\pm\pi/2, 0)$. Our fitting functions $A_b(\phi)$ in equation (5) are such that $A(\pm\pi/2) = 0$ for any value of the fitting parameter b, as required by the existence of a steadily coiling solution.

The optimal value of the fitting parameter b was found to be

$$b = 0.715 \tag{6}$$

This provides a good fit through the numerical data, as shown in figure 4.

The empirical law for $\overline{\kappa}$ in equations (4–6) has been obtained by fitting numerical data for the *translated coiling pattern* coming from a very small region of the phase diagram (darker vertical red bar in the lower left corner of figure 1b). In the main text, we show that a geometrical model based on this law explains the entire phase diagram.

2.2 Robustness with respect to fitting region

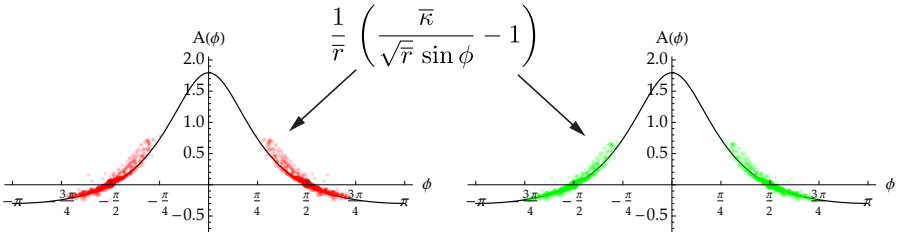

Figure 5: Collapse of the numerical data for $H = 0.5$ (red, left) and $H = 1$ (green, right) onto a master curve $A(\phi)$ defined above in Eq. (5) with $b = 0.715$. In both cases, the datapoints sample the region of the phase diagram corresponding to the translated coiling pattern ($0 < V/U_c(H) < 0.4$). The collapse of the two clouds of points onto the same master curve demonstrates the fact that the result of the fitting procedure for κ is independent on the chosen value of the height H.

The entire fitting procedure described in §2.1 has been repeated for different values of H, each time exploring the range of values of V corresponding to the translated coiling pattern (that is $0 < V/U_c(H) < 0.4$). For all of them, the curvature was found to be well fitted by equation (4). Shown in Fig. 5 are the collapses of the same quantity $\frac{1}{\overline{r}}\left(\frac{\overline{\kappa}}{\sqrt{\overline{r}}\,\sin\phi}-1\right)$ obtained for $H = 0.5$ and $H = 1$, respectively. Both clouds of points collapse onto the same master curve $A(\phi)$ with $b = 0.715$.

Alternatively, we also determined the optimal value of the fitting parameter b for different values of H. Consistent with the fact that the scaled data shown in figure 5 depends very little on H, we found that b varies by less than typically $\sim 5\%$ as H is varied.